nature communications

Article

https://doi.org/10.1038/s41467-025-62836-1

SeeThrough: a rationally designed skull clearing technique for in vivo brain imaging

Received: 2 May 2025

Accepted: 31 July 2025

Published online: 26 August 2025

Check for updates

Xinyi Liu[1,2,8], Motokazu Uchigashima[1,3,8], Ikumi Oomoto[4], Yoshihito Saito[4], Hitoshi Uchida[2], Shinya Oginezawa[1,5], Keiko Masuda[6], Daisuke Satoh[1], Manabu Abe[7], Kenji Sakimura[7], Yoshihiro Shimizu[6], Masanori Murayama[4] ✉, Kazuki Tainaka[2] ✉ & Takayasu Mikuni[1] ✉

Light scattering in the skull limits optical access to the brain. Here we present SeeThrough, a skull-clearing technique that enables simple, high-resolution, and minimally-invasive brain imaging without skull removal. Through systematic screening of over 1600 chemicals, we rationally developed a refractive index-matching solution that combines water- and organic solvent-based components, achieving both high clearing efficiency and biocompatibility. The reagents exhibit minimal brain penetration, maintain tissue integrity, and avoid inflammatory responses. Notably, SeeThrough provides imaging sensitivity and contrast comparable to open-skull window imaging, while permitting minimally-invasive monitoring of brain border macrophages as well as blood and cerebrospinal fluid dynamics. Combined with two-photon imaging, SeeThrough enables spatially and temporally scalable imaging applications in the mouse brain, including ~400 μm deep imaging, one-month longitudinal imaging, and mesoscale, cellular-resolution monitoring of brain activity for network-level analysis. Thus, SeeThrough offers a broadly accessible platform for high-throughput, physiology-preserving imaging of the brain parenchyma and brain-skull interface.

Optical imaging techniques enable researchers to monitor the structural and functional dynamics of cells within the mammalian brain[1]. Two-photon microscopy is widely used for in vivo imaging of the mouse brain, due to its ability for high-resolution imaging at considerable tissue depths[2]. In many cases, two-photon brain imaging relies on open-skull craniotomy, because the skull causes pronounced light scattering and aberrations[3]. Open-skull craniotomy is often followed by implantation of a transparent glass window in the skull, allowing for long-term, high-quality imaging. Nevertheless, cranial window implantation can lead to undesirable consequences, including glial inflammatory responses, intracranial pressure reduction, and the loss of cerebrospinal fluid[4]. These invasive aspects of open-skull surgery potentially compromise the physiological condition of the brain[4].

Several approaches have been developed that do not involve removing the skull. Thinned-skull preparation that allows light penetration enables high-resolution brain imaging[4,5]. However, it is unsuitable for mesoscale imaging due to technical limitations on the size of the thinned skull area. Moreover, the thinned skull bone usually regrows within a few days, affecting imaging quality and hindering long-term observations. Skull optical clearing, which would preserve

[1]Department of Cellular Neuropathology, Brain Research Institute, Niigata University, Niigata, Japan. [2]Department of System Pathology for Neurological Disorders, Brain Research Institute, Niigata University, Niigata, Japan. [3]International Research Center for Neurointelligence (WPI-IRCN), The University of Tokyo, Tokyo, Japan. [4]Center for Brain Science, RIKEN, Wako, Saitama, Japan. [5]Department of Neurology, Brain Research Institute, Niigata University, Niigata, Japan. [6]Laboratory for Cell-Free Protein Synthesis, RIKEN Center for Biosystems Dynamics Research, Kobe, Hyogo, Japan. [7]Department of Animal Model Development, Brain Research Institute, Niigata University, Niigata, Japan. [8]These authors contributed equally: Xinyi Liu, Motokazu Uchigashima. ✉e-mail: masanori.murayama@riken.jp; kztainaka@bri.niigata-u.ac.jp; tmikuni@bri.niigata-u.ac.jp

the brain's physiological integrity and enable longitudinal and mesoscale imaging, has been employed to image the brain through the skull[6–8]. However, the sensitivity, resolution, and longitudinal performance of imaging through the treated skull do not yet match those achieved through open-skull glass windows.

To completely suppress the optical scattering of the skull, a solution that closely matches the refractive index (RI) of the bone tissue (RI = 1.56)[9,10] and minimizes the RI heterogeneity at microscale levels within the tissue is required (RI matching solution, RIMS) (Supplementary Note 1 and Supplementary Fig. 1). While an organic solvent-based RIMS (oRIMS) can achieve the desired high RI of 1.56, its use involves a stringent dehydration process incompatible with living animals[11]. On the other hand, a water-based RIMS (wRIMS) is more biocompatible but offers a lower RI of around 1.52[12,13] due to the limited solute solubility in water. Ideally, a hybrid solution could be used by combining wRIMS and oRIMS (woRIMS), leveraging the advantages of both solutions. However, these solutions are typically immiscible due to their different solubility properties and can easily phase separate in the presence of tissue-derived water present in biological contexts.

In this study, we performed systematic profiling and screening of over 1600 chemicals and identified a compatible pair of organic solvent-based and water-based solutions that are miscible with each other and achieve the targeted RI of 1.56. The resulting technique for skull clearing, termed SeeThrough, is easy to perform, reliably reproducible, and significantly outperforms previous skull clearing methods, which rely solely on water-based solutions (RI = 1.36–1.51). Importantly, SeeThrough provides imaging quality comparable to that of open-skull window imaging while preserving tissue integrity and preventing inflammatory glial activation, thereby enabling minimally invasive imaging of both the mouse brain parenchyma and brain-skull interface. Furthermore, SeeThrough facilitates a range of spatially and temporally scalable imaging applications, such as volumetric brain imaging, longitudinal monitoring of the microscale structural changes in neuronal dendrites, and mesoscale cellular-resolution imaging of brain activity across multiple cortical regions.

Results

Development of the RI matching solution for in vivo skull clearing

To address the challenges of immiscibility and phase separation between wRIMS and oRIMS, we used an aqueous intermediate solvent (AqIS) that could enhance miscibility and prevent phase separation of woRIMS. As an AqIS, we chose the ethanol-based aqueous solution previously used for in vivo experiments[7] (75% ethanol urea-saturated aqueous solution; see Supplementary Note 1). We attempted to identify a compatible pair of wRIMS and oRIMS that are miscible with the AqIS and also with each other (Fig. 1a). Such a hybrid solution would provide a high RI mounting medium that is also biocompatible and thus ideal for in vivo skull optical clearing.

We performed systematic chemical profiling and screening to rationally identify compatible wRIMS and oRIMS (see Supplementary Note 1). To predict solubility between two chemicals, we used Hansen solubility parameters (HSP), based on the idea that chemicals with similar interactions are more likely to dissolve in each other[14]. HSP-based chemical screening for oRIMS candidates (RI > 1.52, close HSP distance, mild odor and toxicity) predicted benzyl alcohol (#1: BA) and veratryl alcohol (#2: VA) to be miscible with 50–75% ethanol *aq* (Fig. 1b and Supplementary Data 1). Next, through chemical profiling using the comprehensive hydration activity dataset[15] (Supplementary Fig. 2 and Supplementary Data 2), we narrowed down 1619 possible wRIMS candidates to 140 aromatic chemicals (high hydration score, estimated RI > 1.58, not deleterious substances) (Fig. 1c). We then performed HSP-based chemical screening (Supplementary Data 3), which predicted two candidates, antipyrine (#0640: ANP) and 2-hydrazinopyridine (#1050), to be miscible with our oRIMS candidates (BA and VA). Since 2-hydrazinopyridine has the problem of discoloration (Fig. 1e), we focused on the pairs of ANP with BA or VA. We confirmed that ANP was miscible with BA or VA while providing an RI of 1.56 (Fig. 1d).

We next assessed the performance of our strategy (combination of the AqIS and woRIMS) using an isolated mouse skull. Both BA/ANP (95.1 ± 3.2%) and VA/ANP (75.7 ± 5.3%) outperformed previous skull clearing reagents[6–8] (9.7–44.4%) in transmittance. Moreover, BA/ANP allowed for a transparency level equivalent to methanol dehydration and BABB clearing (95.8 ± 2.7%), an oRIMS-based protocol known for providing high clearing efficiency in fixed tissue[10] (Fig. 1f). As the woRIMS pair of BA/ANP showed higher performance and cost-effectiveness compared with VA/ANP, we moved forward with this woRIMS hereafter (Fig. 1g).

In vivo brain imaging using SeeThrough

To expedite the penetration of the AqIS and woRIMS into the skull in vivo, we added a permeabilization step (decalcification[12], AqIS and detergent processes) prior to the RI matching, to establish the SeeThrough protocol (Fig. 2a; Supplementary Fig. 3; and Supplementary Data 4, see Supplementary Note 1). The SeeThrough procedure can be completed within 60 min, and images can be obtained immediately afterward. We conducted an in vivo assessment of SeeThrough in living mice. We removed the skin and put a chamber plate over the skull to apply the SeeThrough protocol to the live skull (Fig. 2a and Supplementary Fig. 3). We imaged the structure of blood vessels through one-photon microscopy, as well as that of neurons expressing tdTomato through two-photon microscopy, before and after SeeThrough treatment within the same mice (Fig. 2b). The untreated skull led to strong light scattering and aberrations, resulting in images with low intensity and a poor signal-to-noise ratio, which was assessed using the full width at half maximum (FWHM) of the fluorescent intensity plots along the same structures (Fig. 2b–d). In contrast, the SeeThrough treatment yielded a substantial improvement in imaging sensitivity and contrast (Fig. 2b–d). The imaging sensitivity slightly declined 1.5 h after the SeeThrough treatment, but recovered to the initial level when woRIMS was replaced with a fresh solution 2 h after the treatment (Supplementary Fig. 4). This indicates that the AqIS effect persists for at least 2 h, rendering SeeThrough suitable for physiology experiments lasting several hours.

Comparison with other cranial window techniques

We then examined whether the performance of SeeThrough matched that of an open-skull cranial window, known for offering high imaging quality under two-photon microscopy. In open-skull craniotomy, some laboratories leave the dura mater while others remove it. Thus, we compared the performance of SeeThrough to that of open-skull craniotomy, both with and without durotomy. We found that both the intensity and signal-to-noise ratio for tdTomato were comparable between SeeThrough and open-skull craniotomy, regardless of the presence or absence of the dura mater (Fig. 2b–e and Supplementary Fig. 5). This demonstrates that SeeThrough provides imaging quality on par with that of open-skull craniotomy under both conditions.

We also performed Ca^{2+} imaging to monitor the activity of neurons that expressed jGCaMP8f[16]. We detected spontaneous Ca^{2+} events in dendritic branches in the primary motor cortex, with relative fluorescence changes comparable between SeeThrough- and open-skull craniotomy-based experiments (Fig. 2f–i and Supplementary Movies 1–4). This demonstrates that SeeThrough offers reliable monitoring of neuronal activity even in small cellular structures like dendrites. Furthermore, we imaged the subcellular localization of endogenously expressed proteins, first through the treated skull and then through the open-skull cranial window. To do this, we genetically fused mEGFP to CaMKIIα using a genome editing-based protein labeling method[17,18]. We found that the imaging sensitivity and contrast were comparable between SeeThrough and open-skull craniotomy

https://doi.org/10.1038/s41467-025-62836-1

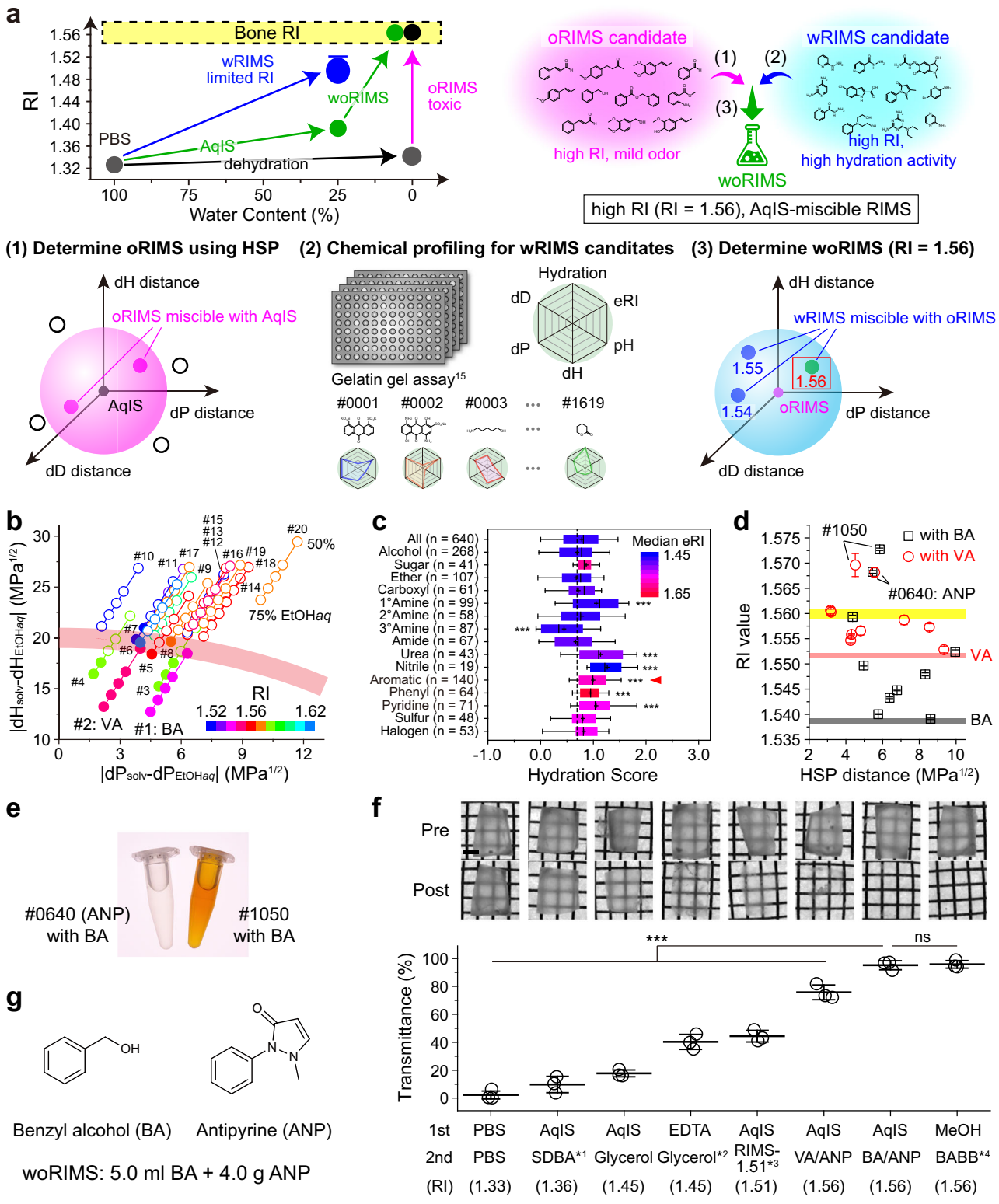

(Supplementary Fig. 6). Thus, SeeThrough enables highly sensitive imaging capable of detecting endogenously expressed proteins.

To determine if SeeThrough is superior to previous methods for live animal applications, we conducted an in vivo sequential comparison of SeeThrough and USOCA[7], a representative switchable skull clearing technique, using the same mice. The imaging sensitivity with SeeThrough was 2.8 times higher than with USOCA, and SeeThrough also provided a better signal-to-noise ratio compared with USOCA (Supplementary Fig. 7). Thus, consistent with the isolated skull experiments (Fig. 1f), SeeThrough outperforms the previous method in terms of in vivo imaging quality.

SeeThrough enables minimally invasive brain imaging

To demonstrate that SeeThrough can be used for minimally invasive brain imaging, we first assessed the potential penetration of SeeThrough reagents through the skull into the cerebral cortex. Using detection assay kits or liquid chromatography-mass spectrometry (LC-MS), we measured the concentration of a series of SeeThrough

Fig. 1 | Development of the RI matching solution suitable for in vivo skull clearing. a Schematic workflow for the development of woRIMS. To develop a skull clearing protocol that achieves both high RI (RI = 1.56) and biocompatibility, an aqueous intermediate solvent (AqIS) was employed, along with a mixture of a wRIMS and an oRIMS that is miscible with the AqIS. dD dispersion parameter, dP polar parameter, dH hydrogen-bonding parameter, eRI estimated RI. **b** A plot of dP and dH distances between a selected set of 20 organic solvents and a 50–75% ethanol aqueous solution. Filled and open circles indicate "miscible" and "immiscible," respectively. The RIs of each organic solvent were displayed using the indicated color code. In a 50–75% ethanol aqueous solution, the miscible radius of the HSP sphere is ~20, indicated by the red curve. **c** Hydration scores for 640 independent, non-detergent, and salt-free chemicals re-analyzed from ref. 11 (Supplementary Fig. 2 and Supplementary Data 2) are displayed as box-and-whisker plots (boxes, 25–75 %; whiskers, 10–90 %; vertical line, median; cross, mean); for each chemical the value plotted is the average of two technical replicates, whereas reference compounds (C#0001–0012) used for normalization are excluded from n. Normality (Kolmogorov–Smirnov, $\alpha = 0.05$) failed only for the alcohol group; therefore, functional groups were compared with the alcohol group by a two-sided Steel test (family-wise $\alpha = 0.05$). Exact results for significant increases: 1° amine ($T = 6.76$, $\rho = 0.194$, $P = 1.88 \times 10^{-10}$), 3° amine ($T = 4.13$, $P = 5.05 \times 10^{-4}$), urea ($T = 4.41$, $P = 1.47 \times 10^{-4}$), nitrile ($T = 4.74$, $P = 3.00 \times 10^{-5}$), aromatic ($T = 5.79$, $P = 9.61 \times 10^{-8}$), phenyl ($T = 3.99$, $P = 9.02 \times 10^{-4}$), and pyridine ($T = 5.08$, $P = 5.41 \times 10^{-6}$); all other groups showed $P > 0.05$. The median estimated refractive index (eRI) for each chemical group is indicated by color coding. **d** A plot of RI values for saturated mixed solutions of the selected wRIMS candidates with BA (black square) or VA (red circle) against the HSP distance between those wRIMS and BA or VA ($n = 3$). The RIs of BA and VA are indicated by the black and red lines, respectively. Data were presented as mean ± SD. **e** The visual appearance of the BA/#0640 and BA/#1050 mixture. **f** Bright-field images of the isolated skull before and after clearing, and a plot of quantified transmittance after clearing. Data were shown as mean ± SD ($n = 3$ independent mice per treatment, one skull per mouse, $^{***}P < 0.001$, ns: $P > 0.9999$, one-way ANOVA with Tukey's multiple comparison test. $P < 0.0001$ for PBS + PBS, AqIS + SDBA, AqIS + glycerol, EDTA + glycerol, and AqIS + RIMS-1.51, and $P = 0.0008$ for AqIS + VA/ANP, when compared with AqIS + BA/ANP). Each solution was referenced from past literature; *1: ref. 7, *2: ref. 6, *3: ref. 8, *4: ref. 10. **g** The chemical structures of benzyl alcohol and antipyrine, and the solution composition of woRIMS. Scale bar, 2 mm (**f**). Credits. Panel **a** includes illustration elements © Shutterstock.com (licensed), not covered by the article's CC-BY 4.0 licence.

reagents in the upper cortical layer beneath the treated skull (Fig. 3a). The levels of EDTA, SDBA, ethanol, and urea were either similar to those in the PBS-treated negative control or below the detection limit (Fig. 3b–e). This demonstrates that AqIS, CUBIC-B, and Detergent have minimal penetration into brain tissue. On the other hand, LC-MS detected <1 μM of ANP, which is less than 0.12% of its IC50 value (860 μM)[19] (Fig. 3f). Since ANP is a commonly used, safe antipyretic analgesic, this minimal concentration indicates that woRIMS has pharmacologically negligible penetration into brain tissue.

We then tested whether SeeThrough perturbed the physiology of the brain by investigating the activation of microglia and astrocytes. Open-skull surgery with durotomy is known to induce inflammatory responses[4]. To test whether SeeThrough also led to inflammation, we monitored the activation of microglia using *Iba1-tdTomato* transgenic mice[20]. We observed a significant accumulation of microglia in the open-skull area 24 h after the durotomy (Fig. 3g, h). In contrast, the intensity of tdTomato remained unchanged 24 h after the SeeThrough treatment (Fig. 3g, h). We also examined the activation of astrocytes through immunohistochemistry using an anti-GFAP antibody[21]. We revealed a substantial increase in the GFAP signal beneath the cranial window 24 h after the durotomy, while the signal under the SeeThrough-treated area remained unaffected (Fig. 3i, j). Furthermore, repeating the SeeThrough procedure three times over seven days did not affect the GFAP signal, indicating that the procedure does not have a long-term impact on astrocyte activation (Fig. 3i, j). On the other hand, open-skull surgery without durotomy did not cause significant inflammatory responses (Fig. 3g–j). However, 7.1% of the blood vessels (6 out of 85 blood vessels in two mice) exhibited to-and-fro blood flow, an abnormality not observed in the SeeThrough experiment (0 out of 96 blood vessels in two mice; Supplementary Fig. 8a–c and Supplementary Movies 5–7). This abnormal blood flow pattern is presumably due to the tissue-deforming pressure from the flat cover glass on the uneven tissue surface. Collectively, SeeThrough enables brain imaging in a less altered physiological state than open-skull craniotomy.

We also evaluated the impact of SeeThrough on overall animal health. We first assessed tissue stability using isolated skulls and found that ten repeated SeeThrough procedures did not compromise tissue stability (Fig. 3k–m). We then examined the effect of SeeThrough on living mice. Seventy-eight percent of the mice survived ten repeated procedures over 1 month, enabling successful imaging (Supplementary Fig. 9a, b). The observed deaths were primarily attributed to impaired recovery from anesthesia, likely due to repeated intraperitoneal administration of anesthetics, or to accidental events such as headplate detachment. One-month survival rates and body weight gain patterns were comparable between mice treated with SeeThrough and those receiving PBS, confirming that the SeeThrough procedure does not negatively impact survival or general health (Supplementary Fig. 9c, d).

Since SeeThrough provides robust tissue preservation and minimal deformation, it is well-suited for imaging not only the brain parenchyma but also delicate brain border regions such as the subarachnoid and perivascular spaces, which are easily damaged or removed during open-skull surgery[22] (Supplementary Fig. 8d). Using *Iba1-tdTomato* mice, we visualized large meningeal and perivascular macrophages in the brain border regions[23], as well as smaller microglia residing in the brain parenchyma, through the SeeThrough-treated skull (Supplementary Fig. 8e, f). In contrast, the open-skull window revealed only small parenchymal microglia with no detectable meningeal macrophages (Supplementary Fig. 8e). SeeThrough also allows for imaging of cerebrospinal fluid flow along the perivascular space, a system highly sensitive to external pressure and disturbance[24] (Supplementary Fig. 8g, h). These minimally invasive imaging capabilities provide straightforward access to the brain-skull interface, facilitating the investigation of neuroimmune interactions and the glymphatic system[25,26].

Spatially and temporally scalable imaging using SeeThrough

Using SeeThrough, we tried a range of spatially and temporally scalable imaging approaches for live brain imaging. First, we performed volumetric brain imaging of EYFP-expressing neurons in the cerebral cortex using *Thy1-EYFP-H* transgenic mice[27]. SeeThrough allows for high sensitivity and contrast imaging at depths of ~400 μm from the brain surface, including layers 1, 2/3, and 5 in the cortex (Fig. 4a, b and Supplementary Fig. 10). Second, we carried out longitudinal imaging to track the dynamic structural changes in neuronal dendrites for 30 days, demonstrating that SeeThrough enables high-quality, dendritic spine level imaging for at least 1 month (Fig. 4c). Notably, SeeThrough is also applicable to long-term imaging of the developing brain at postnatal 3 weeks (Supplementary Fig. 11), a period when the skull and brain growth usually complicates the longitudinal imaging. Third, SeeThrough can be applied to a skull area that potentially encompasses the entire cortex. We conducted "zoom-out" imaging to identify tdTomato-expressing neurons via one-photon microscopy, followed by "zoom-in" imaging to visualize neuronal dendrites via two-photon microscopy (Fig. 4d, e and Supplementary Fig. 12). Thus, SeeThrough can expand the toolkit for large-window imaging[28,29], making it easier to monitor distinct neurons in different cortical areas within the same animal.

https://doi.org/10.1038/s41467-025-62836-1

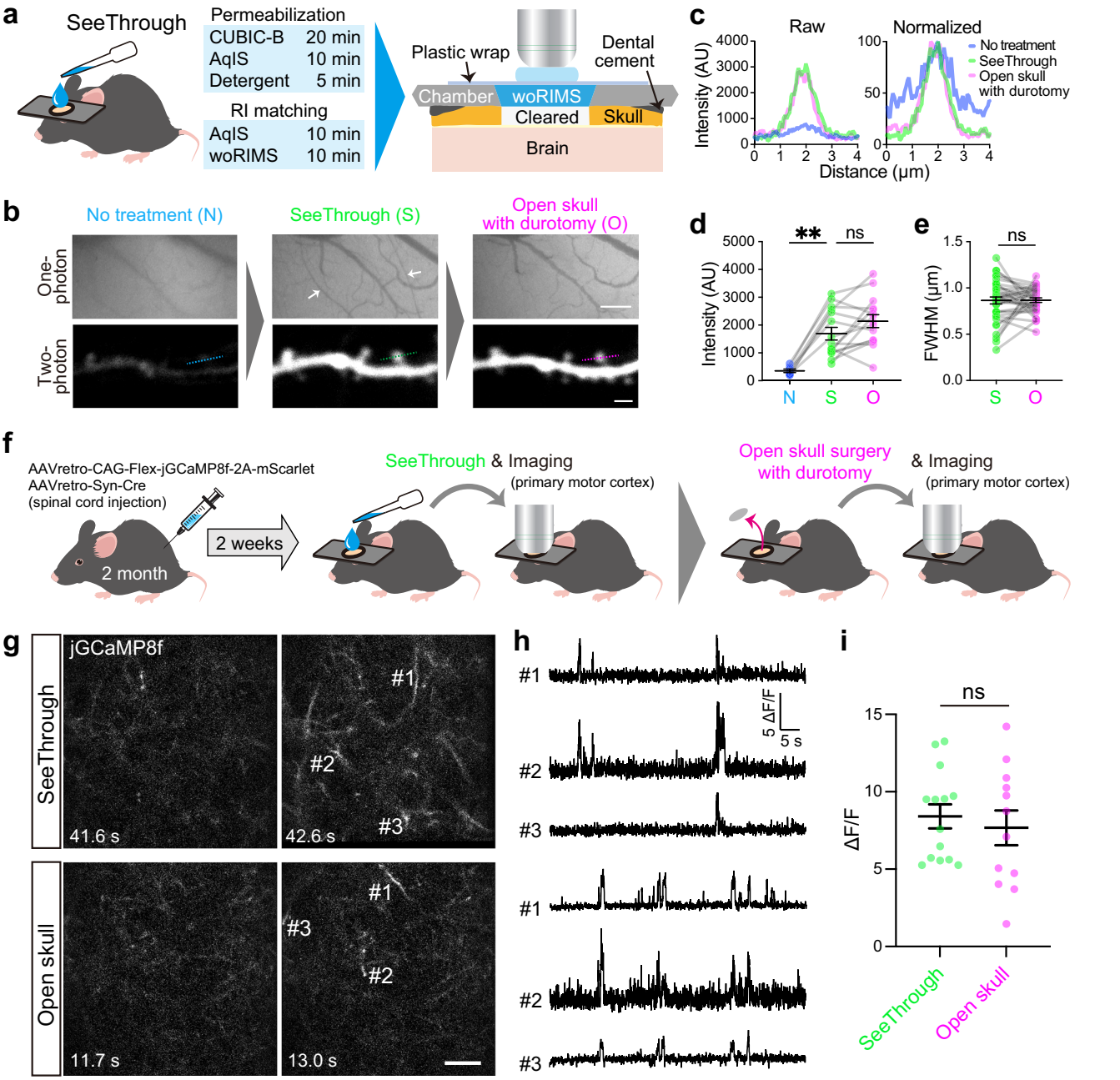

Fig. 2 | In vivo brain imaging using SeeThrough. a Schematic of the SeeThrough procedures. **b** Camera and two-photon images of the vasculature (top) and the tdTomato-expressing neuronal dendrite (bottom) captured through the untreated (left) and SeeThrough-treated (middle) skull and through the open-skull glass window (right) in the same mouse (7 weeks old). Arrows indicate the blood vessels that disappeared after the open-skull surgery. **c** Raw (left) and normalized (right) tdTomato intensity profiles along the dashed lines in (**b**). **d** Comparison of the tdTomato intensity measured from the same dendritic segments before/after SeeThrough and after the open-skull surgery with durotomy (no treatment, $n = 7$ dendritic spines from three mice; SeeThrough, $n = 15$ dendritic spines from five mice; open-skull surgery with durotomy, $n = 15$ dendritic spines from five mice). Plots obtained from the same dendritic segments are connected with gray lines. $^{**}P = 0.0027$, ns not significant ($P = 0.5914$), two-tailed Kruskal–Wallis test. Data were presented as mean ± SEM. **e** Comparison of the full width at half maximum (FWHM) of the tdTomato intensity plots along the same dendritic spines imaged through the SeeThrough-treated skull and the open-skull (with durotomy) glass window ($n = 39$ dendritic spines, $P = 0.7985$, two-tailed Wilcoxon test). Data were presented as mean ± SEM. **f** Schematic of the experimental design. Ca^{2+} imaging was performed using the same mice, first through the SeeThrough-treated skull and then through the open-skull glass window, targeting similar locations and depths in the primary motor cortex. **g**, **h**, Images (**g**) and traces (**h**) for jGCaMP8f signals in dendrites through the SeeThrough-treated skull (top) and the open-skull glass window (bottom). **i** Comparison of ΔF/F between SeeThrough and open-skull experiments (SeeThrough, $n = 14$ dendrites from two mice; open skull, $n = 12$ dendrites from two mice). ns not significant, $P = 0.5604$, two-tailed Mann–Whitney U-test. Data were presented as mean ± SEM. See also Supplementary Movie 1–4. Scale bars, 100 μm (**b**: top), 20 μm (**g**), 5 μm (**b**: bottom). Credits. Panels **a**, **f** include illustration elements © Shutterstock.com (licensed), not covered by the article's CC-BY 4.0 licence.

https://doi.org/10.1038/s41467-025-62836-1

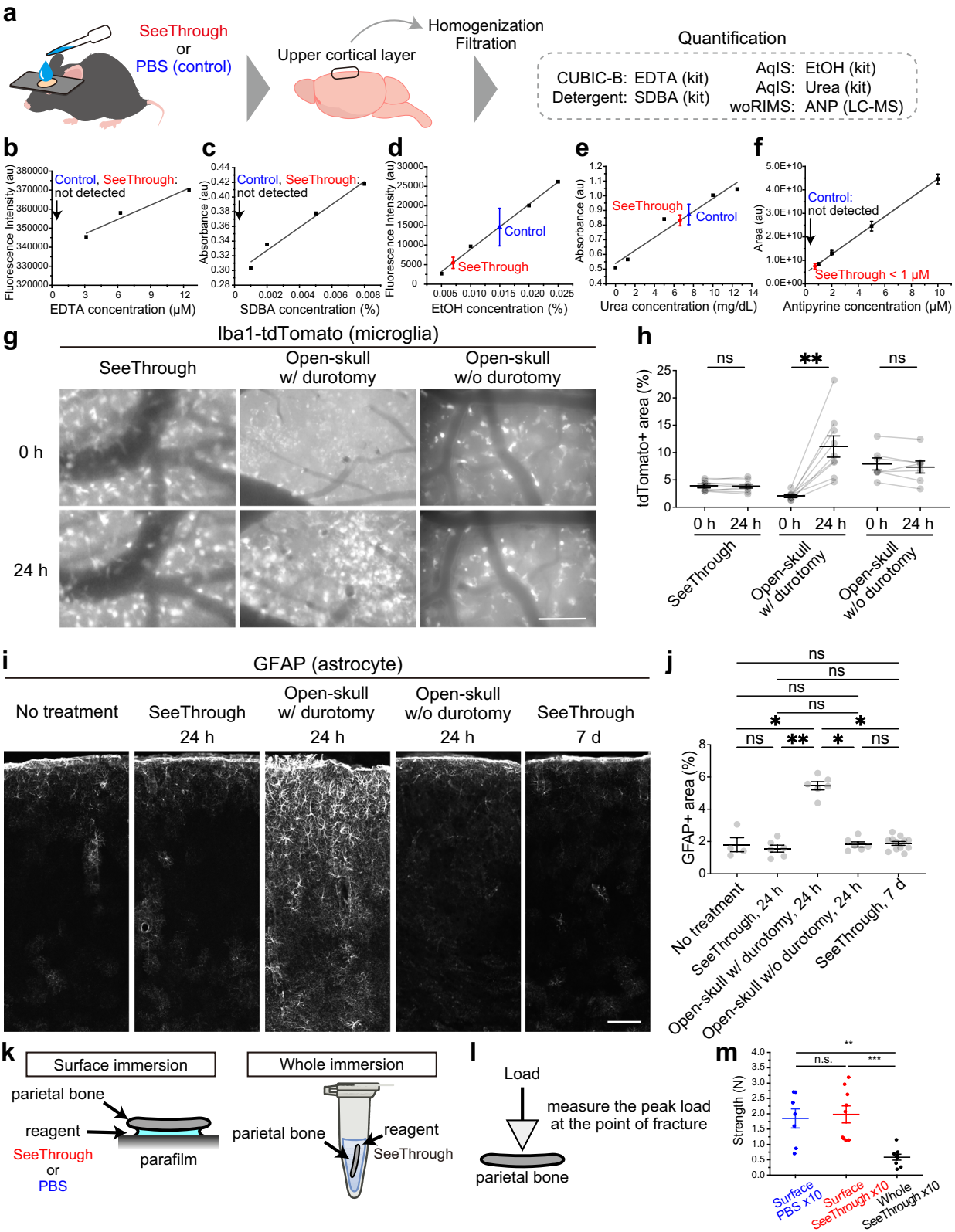

Mesoscale imaging of cellular activity across multiple cortical areas

Monitoring the activity of a large number of neurons from multiple cortical areas provides valuable insights into the functional network architecture of the cerebral cortex. However, open-skull surgery for mesoscale imaging is both highly invasive and technically demanding due to the removal of a significant portion of the skull, which drastically reduces success rates and lowers throughput[30]. To overcome these limitations, we combined SeeThrough and FASHIO-2PM, a fast and wide field-of-view two-photon microscopy technique[31,32] (Fig. 5a). This integrated approach allowed us to conduct extensive monitoring of neuronal activity across multiple cortical areas without the need to remove the skull (Fig. 5b–f). We achieved a 7.65 Hz monitoring of Ca^{2+} activity in 728–2965 neurons, selected based on

Fig. 3 | SeeThrough enables minimally invasive brain imaging. a Schematic of the experimental design. **b**–**f** Calibration curves (black lines) for each chemical to determine its concentration in the brain parenchyma (**b** EDTA; **c** SDBA; **d** EtOH; **e** urea; **f** ANP). Black squares indicate signals measured by standard concentrations for each chemical (standard concentrations: **b** 3.125, 6.25, 12.5 μM; **c** 0.001, 0.002, 0.005, 0.008%; **d** 0.005, 0.010, 0.020, 0.025%; **e** 0, 1.25, 5, 10, 12.5 mg/dl; **f** 1, 2, 5, 10 μM). Blue triangles and red circles indicate the determined concentrations in control (PBS-treated) and SeeThrough-treated samples ($n = 3$), respectively (PBS: **d** 0.015%; **e** 7.54 mg/dl; SeeThrough: **d** 0.007%; **e** 6.63 mg/dl; **f** <1 μM). Detection kits (**b**–**e**) and LC-MS (**f**) were used for the quantification assay. Data were presented as mean ± SEM. **g** Monitoring tdTomato-expressing microglia in the visual cortex in Iba1-tdTomato transgenic mice 0 h (left) and 24 h (right) after the SeeThrough treatment (top), and the open-skull surgery with (w/, middle) or without (w/o, bottom) durotomy. **h** Comparison of the tdTomato fluorescence between 0 and 24 h after the SeeThrough treatment (left, $n = 9$ areas from three mice, $P = 0.5703$, two-tailed Wilcoxon test) and open-skull surgery with (middle, $n = 9$, $^{**}P = 0.0039$, two-tailed Wilcoxon test) or without (left, $n = 7$ from three mice, $P = 0.2968$, two-tailed Wilcoxon test) durotomy. ns not significant. Data were presented as mean ± SEM. **i** Immunofluorescent images of the visual cortex in the coronal brain sections using anti-GFAP antibody. Brains were fixed without any treatment (left), 24 h after the SeeThrough treatment (second left), and 24 h after the open-skull surgery with (middle) or without durotomy (second right). To assess the long-term effect, SeeThrough was performed three times over seven days (on the first, fourth and seventh days) and then the brains were fixed (right). Cortical regions just below the treated areas were examined. **j** Comparison of the GFAP immunoreactivity among no treatment ($n = 4$ areas from two mice), 24 h after the SeeThrough treatment ($n = 6$ from three mice), 24 h after the open-skull surgery without or with durotomy ($n = 6$ from three mice for each), and 7 d after the initial SeeThrough treatment ($n = 12$ from three mice). $^{*}P = 0.0275$ (no treatment vs open-skull with durotomy), 0.0305 (open-skull with durotomy vs SeeThrough, 7 d), and 0.0493 (open-skull with durotomy vs open-skull without durotomy), $^{**}P = 0.0029$, two-tailed Kruskal–Wallis test. Data were presented as mean ± SEM. **k** Schematic of the experimental design. **l** Measurement of the bone mechanical strength. **m** Mechanical strength of parietal bone samples surface-treated for ten sessions with PBS or SeeThrough solutions, and whole-immersed for ten sessions with SeeThrough solutions ($n = 7$ for surface immersion with PBS and $n = 9$ for surface and whole immersion with SeeThrough solutions, $^{**}P = 0.0038$, $^{***}P = 0.0008$, one-way ANOVA with Tukey's multiple comparison test). Data were presented as mean ± SEM. Scale bars, 100 μm. Credits. Panel **a** include illustration elements © Shutterstock.com (licensed) and panel **k** include illustration elements © ACworks/illustAC, not covered by the article's CC-BY 4.0 licence.

morphology, activity, and SNR criteria (see Methods), from three mice that expressed G-CaMP7.09[33], within a 9 mm^2 imaging plane that contained multiple cortical regions (Fig. 5b–f, Supplementary Fig. 13, and Supplementary Movie 8).

To confirm whether the combination of SeeThrough and FASHIO-2PM allows us to examine cortical-wide interactions at the single-cell level, we computed partial correlation coefficients between neurons by conditioning on the mean activity of all neurons. This approach removed the influence of global co-fluctuations and enabled us to evaluate more accurate pairwise relationships between neurons (Fig. 5h, i). We investigated the relationship between inter-neuronal distance and partial correlation values and found that neighboring neurons tended to exhibit higher correlations (Fig. 5j), consistent with previous findings suggesting stronger local interactions[34,35]. We then averaged the partial correlations for each cortical region and used cosine similarity to compare the relationship of inter-regional interaction across mice. Despite differences in the number and distribution of recorded neurons, the average inter-regional relationships were consistently similar across animals (Supplementary Fig. 14). To visualize strongly correlated neuronal pairs and their spatial distribution, we thresholded the partial correlation matrix at the 99th percentile, with the correlations that exceeded this threshold defined as network links (Fig. 5k). Although nearby neurons tend to have higher correlations (Fig. 5j), high-correlation links were not only observed between nearby neurons, but also over long distances (>1500 μm) (Fig. 5l). Furthermore, analysis of the degree distribution of links revealed that a small number of neurons exhibited high numbers of links, suggesting hub-like properties (Fig. 5m). Visualization of these high-degree neurons and their links revealed that they were distributed and coordinated across multiple cortical regions (Fig. 5n). Together, these results demonstrate that our integrated SeeThrough and FASHIO-2PM approach can easily provide a higher-throughput analysis of mesoscale functional networks with single-cell resolution across multiple regions, especially for non-expert surgical operators.

Discussion

In this study, we developed SeeThrough, a rationally designed RIMS-based approach for efficient skull clearing, enabling simple, high-quality, and minimally invasive live brain imaging without skull removal. We showed that SeeThrough provides a range of spatially and temporally scalable imaging applications, including deep imaging up to ~400 μm, 1-month time-lapse imaging, and multi-regional monitoring of brain activity at cellular resolution.

A key innovation of the SeeThrough technique is the development of woRIMS, a rationally designed hybrid reagent that combines the strengths of wRIMS and oRIMS. Unlike conventional tissue clearing reagents[36], which rely solely on either wRIMS or oRIMS due to the immiscibility of water- and organic-based solutions, woRIMS leverages the advantages of both. Through systematic profiling and screening of over 1600 chemicals, we developed woRIMS with a high RI of 1.56 to match the skull's RI, while ensuring biocompatibility to eliminate the need for stringent dehydration processes. This innovation enables not only efficient and minimally disruptive brain imaging through the skull but also introduces a distinctive concept in the development of in vivo tissue clearing strategies.

We showed that the SeeThrough reagents exhibited minimal or pharmacologically negligible penetration through the skull into the brain parenchyma, supporting the minimal invasiveness of the technique. This limited penetration is likely due to the dura acting as an effective diffusion barrier[37] and/or the hydrophobic properties of the reagents, which prevent their entry into the hydrophilic environment of the brain. In addition, we found no evidence of inflammation in the brain or adverse effects on overall animal health, confirming that the SeeThrough technique is safe for use under physiologically relevant conditions.

SeeThrough demonstrated imaging sensitivity and contrast comparable to those achieved with open-skull window imaging, providing a promising alternative for in vivo brain imaging. Specifically, SeeThrough may be the preferred option in several situations. First, SeeThrough offers a practical solution in cases where open-skull surgery is technically demanding—for example, when performed by non-expert operators, when wide field-of-view imaging is required, or when bilateral imaging across venous sinuses is needed, all of which pose challenges for conventional open-skull procedures. While the success of open-skull surgery often depends on operator skill[3,4,22] and requires substantial training to master, SeeThrough enables consistently high success rates even for less experienced users, thereby enhancing experimental throughput and expanding accessibility across laboratories. Notably, it is especially beneficial for advanced applications such as wide field-of-view imaging, where even expert operators often suffer from low success rates for cortex-wide skull removal[30]. Second, SeeThrough is ideal when it is essential to avoid tissue compression or mechanical disturbance, such as in studies of blood and cerebrospinal fluid flow at the brain-skull interface, where maintaining the native tissue architecture is critical. Our results, along with those of others[38], showed that open-skull surgery can alter blood and cerebrospinal fluid

https://doi.org/10.1038/s41467-025-62836-1

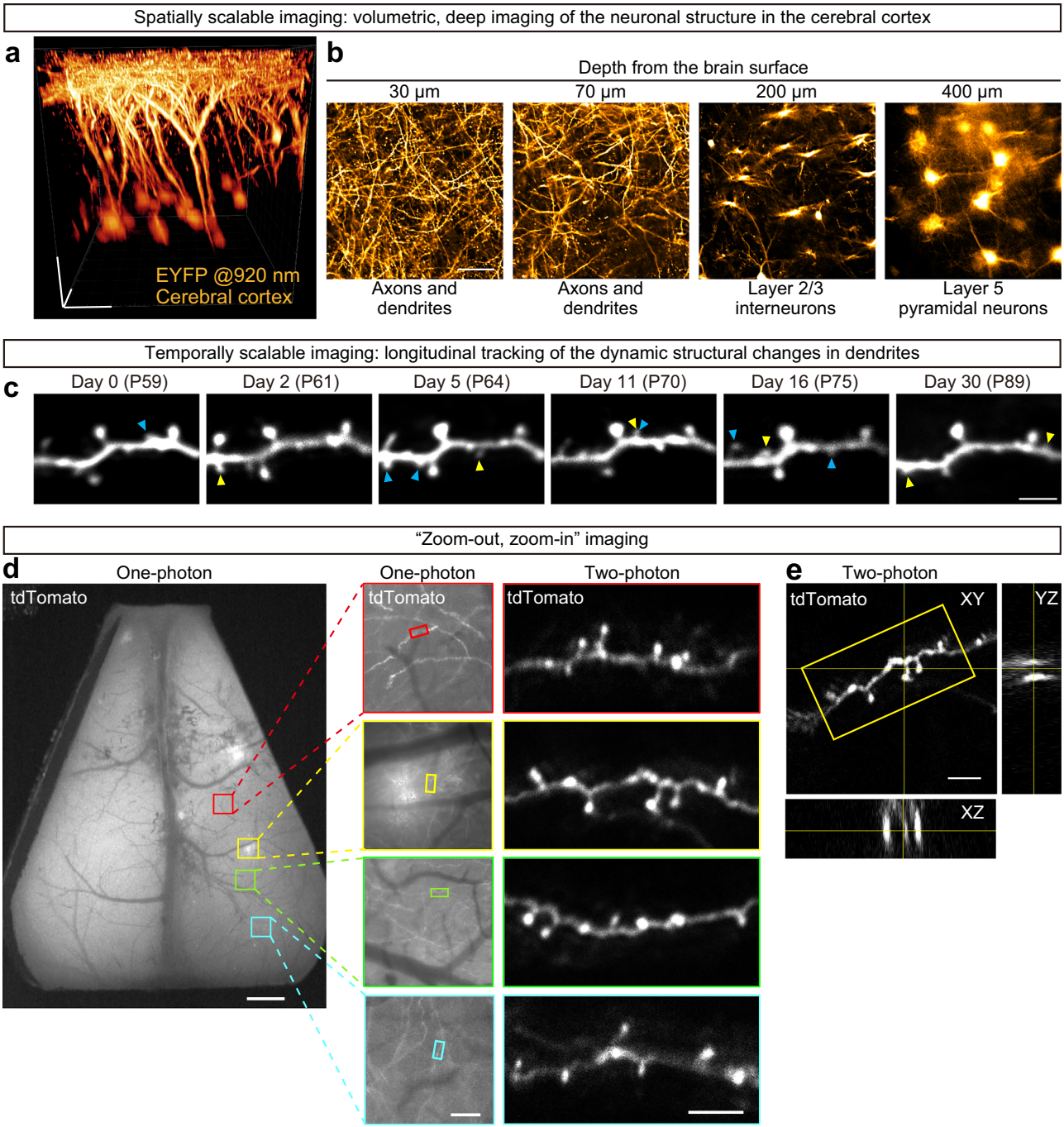

Fig. 4 | Spatially and temporally scalable brain imaging using SeeThrough. a A 3D reconstructed image of the EYFP-expressing neurons in the visual cortex captured through the SeeThrough-treated skull (9 weeks old). **b** Focal plane images of the layer 1, 2/3, and 5 in the cortex. **c** Time-lapse images of the same dendrite captured through the SeeThrough-treated skull. Yellow and blue arrowheads indicate newly formed and eliminated dendritic spines. **d** Wide field-of-view (left) and focused (middle) camera images of the cerebral cortex containing a sparse subset of tdTomato-expressing neurons. Two-photon images of the dendrites located in the colored rectangles in the middle images (right). Three series of dendritic branches from different cortical areas were tested in three mice (3 weeks old). **e** Two-photon images of the dendrite shown in the yellow rectangle in (**d**). The XY, XZ, and YZ images projected with maximum fluorescence intensity exhibit minimal aberration and satisfactory Z resolution. A total of ten dendritic branches (3, 3, and 4 branches per mouse) were tested in three mice (3 weeks old). Scale bars, 5 μm (**c**, **d**, right, **e**), 100 μm (**a**, **b**, **d**, middle), 1 mm (**d**, left).

flow, likely due to the pressure exerted by a flat cover glass on the uneven cortical surface. Thus, although we showed that open-skull surgery without durotomy does not induce undesirable inflammation, it may still disturb intracranial pressure and fluid dynamics, making SeeThrough a more appropriate option in such contexts. Nevertheless, open-skull window imaging still retains certain advantages, including reduced optical aberrations due to the flat glass interface, which can benefit deep brain imaging. In addition, when the dura is left intact, open-skull glass implantation can minimize glial activation and support long-term, high-quality imaging. However, the dura is often inadvertently damaged or removed during surgery, which can trigger coagulation, inflammation, and regrowth of the dura and skull bone[22], ultimately compromising the reliability of physiological imaging. Given that optical clarity in open-skull imaging varies substantially with

https://doi.org/10.1038/s41467-025-62836-1

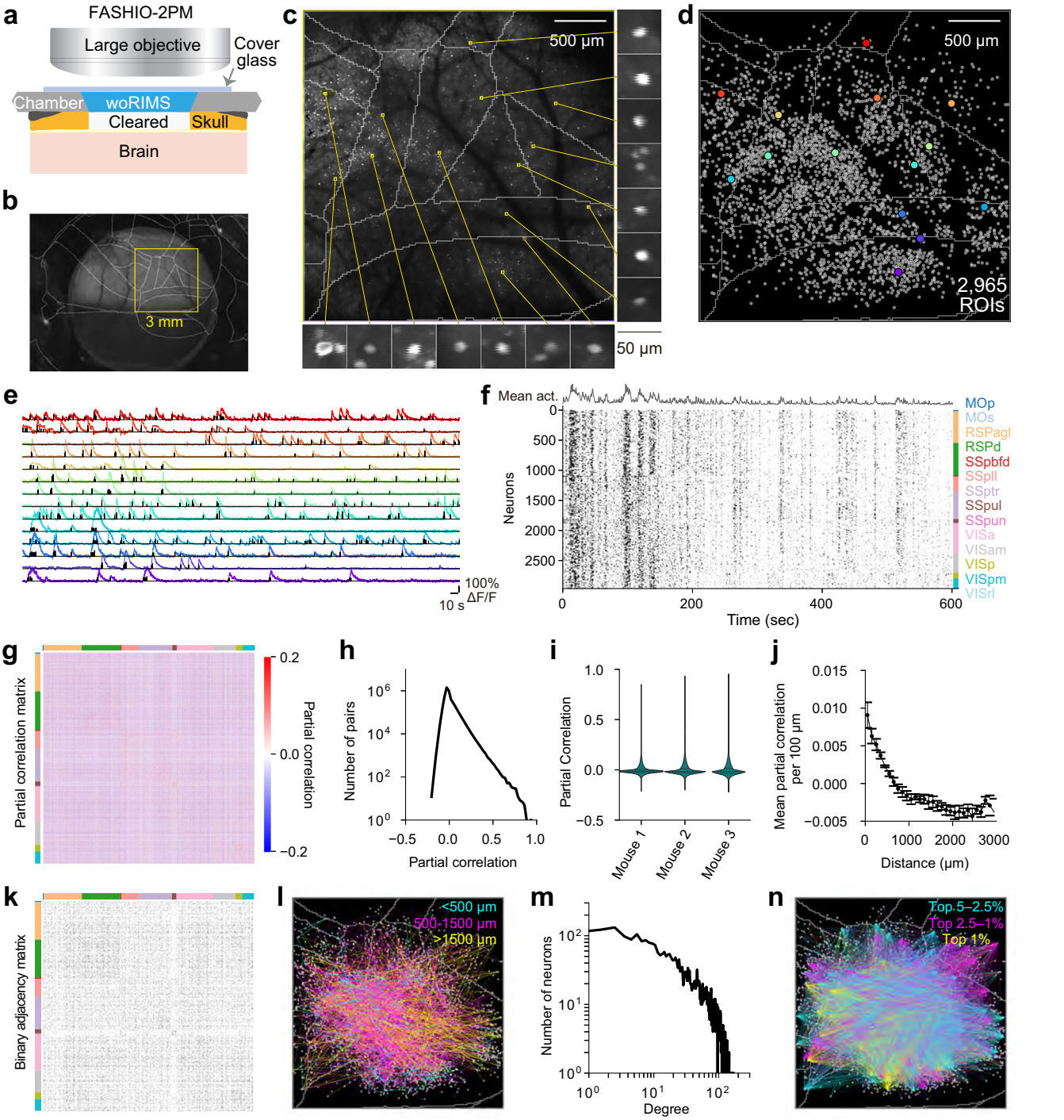

Fig. 5 | Mesoscale, cellular-resolution Ca^{2+} imaging using SeeThrough. **a** Schematic of the integration of SeeThrough and FASHIO-2PM. **b** A camera image. The yellow square indicates the field-of-view (FOV). Overlaid white lines show borders according to the Allen mouse common coordinate framework. **c** A standard deviation projection image for Ca^{2+} imaging of a contiguous full FOV including layer 2 cortical neurons labeled with G-CaMP7.09 at 7.65 Hz sampling rate (150 μm depth from the cortical surface). Representative neurons are shown around the image. **d** An overlaid diagram showing 2965 regions of interest (ROIs). The colors correspond to the Ca^{2+} signals shown in (**e**). **e** Representative Ca^{2+} signals and deconvolved signals from 14 neurons. **f** Z-scored deconvolved signals of individual neurons recorded using FASHIO-2PM across 13 cortical regions in the same representative mouse. Neurons are sorted by region, and the global mean activity of all neurons is plotted above the plot. The color bar indicates the corresponding cortical regions. **g** Partial correlation coefficient matrix quantifies the pairwise relationships between the activities of individual neurons in the representative mouse, after removing the influence of the global mean activity. **h** Distribution of partial correlation coefficients for all neuron pairs in the representative mouse. **i** Distribution of partial correlation coefficients for individual mice. The inner lines indicate the quartile ranges (25th–75th percentiles) and the median. **j** Mean partial correlation coefficients calculated in 100 μm bins as a function of distance, averaged across individuals ($n = 3$ mice). Error bars represent the SEM. **k** Binary adjacency matrix for the same mouse as in (**g**), obtained by thresholding the partial correlation coefficients at the 99th percentile (partial correlation >0.184). **l** Visualization of 2000 randomly selected links from (**k**), color-coded by distance. Links shorter than 500 μm are shown in cyan, those between 500–1500 μm in magenta, and links longer than 1500 μm in yellow. **m** Degree distribution of neurons for the same mouse in (**k**). **n** Visualization of links for high-degree neurons. Links are color-coded based on degree rank: cyan for neurons in the top 5–2.5%, magenta for the top 2.5–1%, and yellow for the top 1%.

surgical skill[3,4,22], the simplicity and robustness of SeeThrough present a significant advantage. Overall, when tissue compression, success rate, and throughput are not major concerns, open-skull window imaging without durotomy could still be a practical choice. Ultimately, researchers can select the most suitable technique based on their specific experimental needs.

One limitation of the SeeThrough method is the need for re-clearing procedures before each imaging session. While we have shown that the AqIS effect lasts for at least 2 h and that repeated procedures do not compromise the skull rigidity, re-clearing steps may not be compatible with certain experimental designs. In this regard, a method using a UV-curable resin to stabilize the transparent skull[8] may be useful for long-term imaging. Although the previously used resin had a lower RI of 1.51 than the skull, a high-RI resin compatible with the SeeThrough method could maintain skull transparency and provide a promising strategy for future studies.

Due to its simplicity, minimal invasiveness and high versatility, SeeThrough will find applications across various neuroscience fields to explore brain physiology and pathophysiology. For example, unlike open-skull glass implantation, which deforms the natural curvature of the brain surface, SeeThrough preserves the physiological integrity of tissue structures beneath the skull, such as the vasculature and subarachnoid space. This preservation makes SeeThrough particularly well-suited for live imaging of neuroimmune interactions[25] and the glymphatic system dynamics[26] in the brain-skull interface. Its ability to visualize cerebrospinal fluid flow along the perivascular space without the influence of tissue compression highlights the potential of SeeThrough to advance research in this area. In the future, the incorporation of adaptive optics to correct spherical aberrations arising from skull curvature[39], or the integration with three-photon microscopy[40], holds the potential to enhance the overall imaging quality.

Methods

Animals

Animal care and experimental protocols were approved by the Animal Experiment Committee of Niigata University or RIKEN and were carried out under the Guidelines for the Care and Use of Laboratory Animals (protocol number: SA01664). Wild-type mice (C57BL/6JJmsSlc; Japan SLC, Shizuoka, Japan), CAG-SpCas9 transgenic mice (RIKEN BRC, #RBRC11579), Thy1-EYFP-H transgenic mice (Jackson Laboratory, #003782)[27] and Iba1-tdTomato transgenic mice[20] were used. Both male and female mice were used and randomly assigned to experimental groups. In all the experiments, the mice were housed in a 12-h-light/12-h-dark light cycle environment with ad libitum access to food and water.

AAV vector production

Custom AAV vectors were produced by Addgene, Penn Vector Core at the University of Pennsylvania, or Virus Vector Core at the program for Brain Mapping by Integrated Neurotechnologies for Disease Studies (Brain/MINDS). AAV-CAG-FLEX-tdTomato (Addgene, #51503), AAV-Syn-Cre (Brain/MINDS, #FA-022), and AAV-HDR-mEGFP-CaMKIIα[18] were pseudotyped with serotype 1. AAV-SynImCMV-Cre (Brain/MINDS, #GA-021) and AAV-CAG-Flex-jGCaMP8f-2A-mScarlet were pseudotyped with the retrograde serotype[41]. The AAV-CAG-Flex-jGCaMP8f-2A-mScarlet plasmid was constructed from the pGP-AAV-syn-FLEX-jGCaMP8f-WPRE plasmid (Addgene, #162379). G-CaMP7.09[33] was subcloned into the synapsin I (Syn)-expressing vector from the pN1-G-CaMP7.09 vector construct. AAV-DJ-Syn-G-CaMP7.09-WPRE was produced as previously described[42].

AAV injection

For viral transduction into neonatal brains in vivo, wild-type or CAG-Cas9 mice at P0-2 were cryoanesthetized for 2–3 min before injection, and gently held by hand. A mixture of AAV-CAG-FLEX-tdTomato (1.0×10^{12} GC/ml) and AAV-Syn-Cre ($0.6–1.2 \times 10^{9}$ GC/ml) for a sparse neuron imaging or AAV-HDR-mEGFP-CaMKIIα (1.0×10^{13} GC/ml) for endogenous CaMKIIα imaging, together with Fast Green (0.1 mg/ml, Sigma-Aldrich), was injected into the unilateral cerebral cortex by a hand-held microdispenser (Drummond). To obtain a large injected area, the total volume of 2–4 μl viral solution was administrated for multiple injection sites 1–2 mm separate from each other. The injection result was confirmed by coloring the entire cortex with Fast Green. After injection, the pups were placed on a heat blanket for several minutes and then returned to their mother.

For local calcium imaging, adult mice at postnatal 6–7 weeks were stereotaxically injected into the spinal cord at the lumbar levels with a mixture of AAV-SynImCMV-Cre (6.0×10^{11} GC/ml) and AAV-CAG-Flex-jGCaMP8f-2A-mScarlet (3.3×10^{13} GC/ml) under anesthesia with a mixture of medetomidine, midazolam, and butorphanol. A viral solution of 0.3–0.5 μl was administered at two or three injection sites per mouse. Imaging was performed 2 weeks after the injection, in which jGCaMP8f was retrogradely expressed in the primary motor cortex.

AAV injections and surgery for FASHIO-2PM imaging were performed using previously described protocols[31,32] with slight modifications. Neonatal mice (postnatal day 0–2) were collected from their cages and anesthetized on ice (cryoanesthesia) for 2–3 min before injection, and then mounted in a neonatal mouse head holder (custom-made, NARISHIGE). The AAV (diluted to 4.0×10^{12} GC/ml with 1x phosphate buffer saline (PBS), 4 μl per pup) was injected into the neonatal cortex using a glass pipette (Q100-30-15, Sutter Instrument) with a diameter of 45–50 μm. The injection site was located at a depth of 0.25–0.3 mm in the frontal area. The injection procedure was completed within 10 min after cryoanesthesia initiation, and the pups were warmed until their body temperature returned to normal. After the pups began to move, they were returned to their mothers.

In vitro chemical screening

Each Hansen solubility parameter (dD, dP, and dH) was calculated using HSPiP software (4th edition; https://www.hansen-solubility.com/HSPiP/). For the liquids of oRIMS and woRIMS in Fig. 1b, d, we measured the RI using an Abbe refractometer (DR-A1, Atago). Since many wRIMS candidates are solids, it is challenging to measure their RI in the same way. Therefore, the eRI of wRIMS was calculated using HSPiP software.

To select oRIMS candidates miscible with AqIS, we listed 20 organic solvents with HSP distances close to a 50–75% ethanol *aq*, an RI of 1.52 or higher, and mild toxicity and odor. Chemical ID numbers were assigned in order of proximity to the HSP distance against a 75% ethanol aqueous solution. To investigate the miscibility of each organic solvent with an ethanol-water solution, equal volumes of the organic solvent and ethanol-water solution were mixed and vigorously stirred. If a distinct interface was observed, it was evaluated as “immiscible”; if no interface was visible and the solution appeared homogeneous, it was assessed as “miscible” (Fig. 1b).

To select wRIMS candidates, we performed chemical profiling on the dataset obtained from comprehensive chemical screening based on the previous gelatin assay[15]. After excluding chemicals that could not be measured for the hydration score and those with a hydration score below −1.5 (Supplementary Fig. 2a), acidic chemicals inducing pH-dependent gel swelling were also excluded (Supplementary Fig. 2b). The remaining chemicals were classified into surfactants, salts, and other chemicals (Supplementary Fig. 2c). We then performed functional analysis on non-detergent and salt-free chemicals according to the previous paper (Fig. 1c)[11]. We selected wRIMS from among the aromatic group with high hydration scores and high eRIs. BA and VA, which are candidate oRIMS, have RIs smaller than 1.56. To adjust the woRIMS with an RI of 1.56, it is necessary for wRIMS to have a high RI. Therefore, we narrowed down the wRIMS candidates to ten chemicals

based on the eRI, hydration score, and HSP distance against BA or VA. To determine the wRIMS paired with BA or VA, we adjusted saturated solutions of BA or VA with ten candidate chemicals and measured the RI of the resulting supernatant (Fig. 1d). The mixture of 2-hydrazinopyridine (#1050) with BA or VA exhibited a red color, so the mixture of antipyrine (#640) with BA or VA was chosen as a candidate for woRIMS.

Next, we investigated whether RI matching using woRIMS via AqIS could render the mouse skull transparent. The isolated mouse skull was immersed in 1.5 ml of the first solution, then gently shaken by a rotator (NRC-30D, Nissin Rika) at room temperature for 10 min. In the first solution, we used AqIS [a urea (35905-35, Nacalai Tesque)-saturated 75% ethanol aqueous solution] or a 10% (w/v) EDTA disodium (343-01861, Fujifilm Wako Pure Chemical) aqueous solution (pH 7.0). Subsequently, the skull was immersed in 2 ml of the second solution with gentle shaking at room temperature for 5 min. In the second solution, we used a 567 mM SDBA aqueous solution [an aqueous solution of dodecylbenzenesulfonic acid (44198-250 ML, Sigma) neutralized with NaOH*aq*], 80% glycerol (17018-25, Nacalai Tesque) aqueous solution, RIMS-1.51 [a mixture of 10 ml of Iohexol 350 (Hikari Seiyaku), 4 g of urea (35905-35, Nacalai Tesque), and 7.5 g of Nycodenz (18003, Serumwerk Bernburg AG) with an adjusted RI value of 1.513], BA/ANP [a mixture of 5 ml of benzyl alcohol (B2378, Tokyo Chemical Industry) and 4 g of antipyrine (D1876, Tokyo Chemical Industry)], or VA/ANP [a mixture of 5 ml of veratryl alcohol (V0020, Tokyo Chemical Industry) and 2 g of antipyrine]. In the methanol-BABB clearing, the skull was sequentially immersed in 1.5 ml of 60–80–100–100% methanol (137-01823, Fujifilm Wako Pure Chemical), with gentle stirring at room temperature for 5 minutes at each step. Subsequently, it was immersed in 2 ml of BABB [a mixture of 0.67 ml of benzyl alcohol and 1.33 ml of benzyl benzoate (B0064, Tokyo Chemical Industry)] and stirred at room temperature for 5 minutes. Shortly afterward, we captured photographs of the samples using the digital camera (EOS Kiss X8i, Canon) under LED lighting (TPAP1B-2450NCW, Hikari Shop) and quantified the transmittance of the skull by analyzing these images using ImageJ software (Fig. 1f).

The SeeThrough reagents

To achieve rapid in situ clearing of the living mouse skull, we introduced a permeabilization step consisting of decalcification and delipidation prior to the RI matching step with woRIMS. Referring to the previous papers[7,11], decalcification was performed using CUBIC-B [an aqueous solution containing 10 wt% ethylenediaminetetraacetic acid (E0084, Tokyo Chemical Industry) and 15 wt% imidazole (I0001, Tokyo Chemical Industry)]. Delipidation was achieved with Detergent, a 567 mM SDBA aqueous solution. AqIS was prepared using a urea-saturated 75% ethanol aqueous solution. woRIMS was prepared by mixing 5 ml of benzyl alcohol with 4 g of antipyrine. See Supplementary Data 4 for the detailed list of the SeeThrough reagents.

The SeeThrough procedures

Mice at postnatal 3–12 weeks were anesthetized by intraperitoneal injection with a mixture of medetomidine (0.75 mg/kg of body weight; Zenoaq), midazolam (4.0 mg/kg of body weight; Sandoz), and butorphanol (5.0 mg/kg of body weight; Meiji Seika Pharma) or inhalation of 1–2% isoflurane at a flow rate of 0.1 l/min (abbvie). The skull was exposed by cutting off the scalp and removing soft tissues on the top and sides of the skull. Saline (Otsuka) was used to keep the skull surface moist during the procedure. A 1-mm-thick metal headplate with a ø5-mm-round hole (CP01, Narishige) or a custom-shaped one (Supplementary Fig. 12) to expose the entire skull (Height: 8 mm, width: 7 mm) was fixed on the skull with a dental cement (Super Bond C&B, Sun Medical) to make a skull chamber (Fig. 2a). For the skull clearing, the skull was permeabilized by filling up the skull chamber with 50 μl of CUBIC-B for 20 min, AqIS for 10 min, and Detergent for 5 min. The skull chamber was further treated with 50 μl of AqIS for 10 min and woRIMS for 10 min to adjust the refractive index (RI) to 1.56 across the skull chamber. CUBIC-B and AqIS were changed with fresh solutions every 5 min. Prior to imaging, the skull chamber was emptied, and filled with 50–100 μl of fresh woRIMS to the level of the headplate's top surface to maximize the clearing effect of woRIMS. A piece of transparent polyvinylidene chloride plastic wrap with a thickness of ~10 μm (Asahi Wrap, Asahi Kasei) was placed on the surface of the cleared skull to seal the skull chamber, preventing woRIMS from being mixed up with the immersion water for imaging. After imaging, the cleared skull was washed with AqIS and sterile water briefly, followed by the application of betamethasone/gentamicin ointment (Rinderon VG, Shionogi). The ointment was used as a precautionary measure to prevent potential bacterial infection and inflammation, although we did not encounter any significant infection or inflammation that affected imaging outcomes. The skull was then protected with a waterproof sheet until the next imaging. Finally, mice were recovered from anesthesia by intraperitoneal injection with antisedan (0.75 mg/kg of body weight; Zenoaq) and returned to the home cage. For longitudinal imaging, the skull was treated for permeabilization and RI matching at every imaging. To compare SeeThrough with USOCA[7], the same skull was sequentially treated with the USOCA and SeeThrough procedures. For the USOCA procedure, the skull chamber was filled with 100 μl of a urea-saturated 75% ethanol aqueous solution for 10 min and a 567 mM SDBA aqueous solution for 5 min, and then sealed with a piece of Asahi Wrap to separate the clearing solution from the immersion water for imaging. After imaging, the skull was treated with the SeeThrough procedure. All the skull clearing procedures were performed at room temperature (20–25 °C).

Quantification of SeeThrough reagents infiltrating into the brain parenchyma

We developed a quantitative evaluation system to assess the penetration of each chemical (EDTA, SDBA, ethanol, urea, and ANP) used in each step of SeeThrough into the brain parenchyma. For the sample preparation, the upper cerebral cortex of the right brain parenchyma of 8-week-old mice was excised and suspended with 500 μl of PBS using an ultrasonic disrupter UR-21P (TOMY Digital Biology). The suspension was then centrifuged (19,500 × *g*, 4 °C, 10 min), and the collected supernatant was filtered through a 0.22-μm Millex-GP (SLGPR33RS, Merck). The quantification of EDTA was performed using the MicroMolar EDTA Assay Kit (ProFoldin), SDBA with the PONAL KIT-ABS (Dojindo), ethanol with the Amplite Ethanol Quantitation Kit (AAT Bioquest), and urea with the QuantiChrom Urea Assay Kit (DIUR-100, BioAssay Systems). Mass spectrometric analysis of ANP was performed using an Orbitrap mass spectrometer (Orbitrap Q Exactive, Thermo Fisher Scientific) equipped with a nanospray ion source (Nanospray Flex, Thermo Fisher Scientific) and a nano-LC system (UltiMate 3000, Thermo Fisher Scientific). We obtained the calibration curve by adding specified concentrations of chemicals to untreated mouse-derived samples and quantifying them using the kits or LC-MS. We used the calibration curve to determine the concentration of each chemical in the brain parenchyma, quantitatively comparing the concentrations between the SeeThrough treatment and the PBS (negative control) treatment.

For the quantification of EDTA, a sample of 200 μl was prepared using 100 μl of filtered brain sample according to the manual. We measured the fluorescence intensity using a microplate reader ARVO MX (PerkinElmer, MA, USA) equipped with a 485 nm excitation filter and a 535 nm emission filter.

For the quantification of SDBA, we performed the quantification with a modified manual using a different solution volume. One tablet of the kit's chromogenic reagent was dissolved in 25 ml of PBS, and 2.5 ml of this solution was mixed with 100 μl of filtered brain sample and 2.4 ml of PBS. After adding 1 ml of the kit's extraction solution and

stirring, the mixture was left to stand at room temperature overnight. The upper organic layer (200 μl) was collected, and absorbance was measured using a microplate reader ARVO MX equipped with a 560 nm absorbance filter.

For the quantification of ethanol, a 1 mM final concentration of 4-Methylpyrazole (M0774, Tokyo Chemical Industry) was added immediately after excising the cerebral cortex to eliminate the influence of endogenous alcohol dehydrogenase. A sample of 100 μl was prepared using 50 μl of filtered brain sample according to the manual. We measured the fluorescence intensity using a microplate reader ARVO MX equipped with a 555/38 nm bandpass excitation filter and a 590/20 nm bandpass emission filter.

For the quantification of urea, a sample of 250 μl was prepared using 50 μl of filtered brain sample according to the manual. We measured the absorbance using a microplate reader ARVO MX equipped with a 520/8 nm bandpass absorbance filter.

For the quantification of ANP, 300 μl of acetonitrile was added to 100 μl of filtered brain sample to precipitate the proteins, and 200 μl of the supernatant was collected. The supernatant was dried and redissolved in 0.1% trifluoroacetic acid, and 1 μl of each sample was applied to the nano-LC system. Samples were concentrated using a trap column (0.075 × 20 mm, 3 μm, Acclaim PepMap 100 C18, Thermo Fisher Scientific) and then separated using a nanocapillary column (0.075 × 150 mm, 3 μm, C18, NTCC-360/75-3-153, Nikkyo Technos) using two mobile phases A (0.1% formic acid) and B (acetonitrile and 0.1% formic acid) with a gradient (1% B for 5 min, 1–40% B in 35 min, 40–90% B in 1 min, and 90% B in 4 min) at a flow rate of 300 nL/min. Elution was directly electrosprayed (2.2 kV) into the MS (positive mode, scan range of 70–300 m/z, 70,000 FWHM resolution). For data analysis, an extracted ion chromatogram (XIC) for m/z 189.102 was generated using Xcalibur Qual Browser (Thermo Fisher Scientific), and the resulting peak area values were exported.

Measurement of tissue stability

We established an experimental system to measure the mechanical strength of bone tissue to evaluate tissue stability after repeated SeeThrough treatments. A series of 5 μl SeeThrough reagent or PBS was placed on parafilm, and the surface of the parietal bone of 8-week-old mice was immersed according to the actual SeeThrough protocol at room temperature. This treatment mimics the typical SeeThrough protocol in living mice. We prepared parietal bone samples by conducting ten sessions of the surface immersion SeeThrough treatment and ten sessions of the surface immersion PBS treatment (treated with PBS for the same duration instead of all SeeThrough reagents). In addition to the surface immersion samples, whole immersion samples were prepared for comparison. A series of 800 μl SeeThrough reagents were prepared, and the parietal bone was immersed in the solutions, replacing them in the same order (with the same processing time) as specified in the SeeThrough protocol. The mechanical strength of the bone samples was evaluated using a texture analyzer (TEX-100N, Japan Instrumentation System Co., Ltd.). A holder equipped with double clips to securely hold the parietal bone was custom-made. The parietal bone was fixed at both ends with double clips, and a wedge-shaped plunger was used to apply load to the center of the bone until fracture, measuring the peak load at the point of fracture.

Open-skull surgery

For comparison, seven mice were subject to the open-skull surgery after the SeeThrough procedure. Under anesthesia with a mixture of medetomidine, midazolam, and butorphanol or isoflurane, craniotomy was performed with a ø5-mm biopsy punch (BP-50F, Kai Medical) over the visual cortex. The dura mater was picked up and removed from the window area with a thin syringe needle (Carpule 35 G, Kulzer) in five mice ("with durotomy"), while left on the brain in two mice ("without durotomy"). Then, the cranial window was implanted with a double-layered glass coverslip with two round coverslips (6.5 mm diameter and No. 1, 0.12-0.17 mm thickness; 4 mm diameter and No. 5, 0.45-0.6 mm thickness, Matsunami Glass) glued with a UV curing adhesive (PN6110, Norland Products), and sealed with cyanoacrylate glue (Aron-alpha, Toagosei).

Tracing of cerebrospinal fluid and blood vessels

For cerebrospinal fluid (CSF) tracing, mice were anesthetized with a mixture of medetomidine, midazolam, and butorphanol, and heated on a heat mat (Vivaria) to maintain their body temperature at 37 °C. A 30 G cannula was implanted into the cisterna magna, and connected to a 10 μl Hamilton syringe controlled by a microsyringe pump (World Precision Instruments). Next, the SeeThrough procedure was performed to clear the skull. The cisterna magna was then injected with 10 μl of 5.0% (w/v) 4-kDa dextran-conjugated FITC dye (#46944, Sigma) for 30 min.

Vascular tracing was done just before imaging cranial windows prepared by the SeeThrough procedure or open-skull surgery without durotomy. For dual tracing of CSF and blood vessels, CSF tracing was followed by vascular tracing. Under anesthesia with a mixture of medetomidine, midazolam, and butorphanol, mice were retro-orbitally injected with 50 μl of 2.5% 70-kDa dextran conjugated with Fluorescein Isothiocyanate (FITC) dye (FD70, TdB labs) or Texas Red (D1864, Thermo Fisher).

One-photon live imaging

Blood vessel images via the intact, transparent, and open-skull window was acquired with an upright one-photon microscope (MZ FLIII, Leica) with a 75 W xenon light source and cooled CCD camera (ORCA-R2 C10600, Hamamatsu Photonics). Images (672 × 512 pixels) were acquired with a zoom factor of five via BP450-490 excitation and LP515 emission filters.

Microglia imaging from Iba1-tdTomato transgenic mice at postnatal 4–6 weeks was performed with an upright fluorescent microscope system (DM6000CS, Leica) equipped with a 20x water immersion objective (HCX PL APO; numerical aperture = 1.0, working distance = 2.0 mm, Leica) and digital CMOS camera (Digital Sight 1000, Nikon) or an upright fluorescent microscope (Bergamo II, Thorlabs) equipped with a 25x water immersion objective (XLPLN25XWMP2; numerical aperture = 1.05, working distance = 2.0 mm, Olympus), 565 nm LED light (M565L3, Thorlabs), and digital CMOS camera (CS235MU, Thorlabs). Images (1280 × 960 or 1920 × 1200 pixels) were taken with a 580 nm dichroic mirror, 515–560 nm band pass and 590 nm long pass emission filters.

Before FASHIO-2PM imaging, skull images over the implanted head plate were acquired from one-photon macroscopic imaging after surgery to estimate the brain regions. The FOV was 13.3 × 13.3 mm and the image resolution was 1024 × 1024 pixels after 2x spatial binning. The intensity of the excitation light from a blue LED source (LEX2-B-S, Brain Vision Inc.) and the gain and exposure time of the sCMOS camera (Zyla 5.5, Andor) were tuned so that none of the pixels were saturated.

Two-photon live imaging

Two-photon imaging was performed with a resonant-galvo scanning microscope (Bergamo II, Thorlabs) equipped with a 25x water immersion objective (XLPLN25XWMP2; numerical aperture = 1.05, working distance = 2.0 mm, Olympus) and two fixed femtosecond fiber lasers (ALCOR 920-4 XSight and ALCOR 1064-5 XSight, Spark Lasers) at the excitation laser wavelength of 920 nm and 1064 nm, respectively; or another resonant-galvo scanning microscope (TCS SP5 MP, Leica) equipped with a 20x water immersion objective (HCX PL APO, Leica) and a Ti:Sa mode-locked femtosecond laser (Chameleon Vision, Coherent) at the excitation laser wavelength of 920 nm. The laser power was set to 9–397 mW at the front of the objective lens (Supplementary Data 5 and Supplementary Fig. 10). Green and red

fluorescent signals were collected using a band pass filter (525/50 nm for the green channel, 607/70 nm for the red channel) and detected with GaAsP PMTs. The acquisition of dendritic images from the cortex was done with a zoom factor of 8x, an averaging number of 64x, and an image size of 512 × 512 or 1024 × 1024 pixels. Calcium imaging or CSF/vascular tracer imaging was done with a zoom factor of 2-4x, image size of 512 × 512 pixels, and frame rate of 30 frames/s. For the time of CSF tracer imaging (t), we defined the time to end the injection of a CSF tracer as t = 0. Mice were under the awake condition for calcium imaging, while anesthetized with a mixture of medetomidine, midazolam, and butorphanol for the other imaging.

Wide field-of-view two-photon calcium imaging

In vivo two-photon imaging was performed using a custom-designed wide field-of-view two-photon laser scanning microscope (FASHIO-2PM)[32]. To observe the spontaneous neural activities in awake mice under the microscope, the mice were fixed in a custom-made stage box (ExPP Co., Ltd.) by firmly screwing the head plate to the stage, and covered with an enclosure to maintain body temperature. Since the objective lens of FASHIO-2PM system is dry immersion, a cover glass (No.1 glass, Matsunami, custom-made) was placed over the hole in the head plate filled with the SeeThrough reagent so that the observation surface was flat. Fluorescence was observed in the somas of layer 2/3 neurons (150 μm below the cortex surface). G-CaMP7.09 was excited at 920 nm using a tunable Ti:Sa laser (Maitai DeepSee, Spectra Physics) and the laser power was set to 180–200 mW at the front of the objective lens. The fluorescence of G-CaMP7.09 was detected with a GaAsP PMT in the range of 515–565 nm. All imaging sessions were performed at 7.65 frames/s with 2048 × 2048 pixels using custom-built software (Falcon, Nikon) and were saved as 16-bit monochrome tiff files.

ROI detection and signal processing of FASHIO-2PM data

We used the Suite2p algorithm (http://github.com/cortex-lab/Suite2P)[43] to identify the ROIs corresponding to single neurons, and to extract their fluorescence time courses. The fluorescence time course $F_{\mathrm{ROI}}(t)$ of each ROI was calculated by averaging all pixels within the ROI at a given time point t, and the fluorescence signal of the cell body was estimated as $F(t) = F_{\mathrm{Roi}}(t) - r \times F_{\mathrm{neuropil}}(t)$, where $r = 0.7$. The ΔF/F was calculated as $\Delta F/F(t) = (F(t) - F_0(t)) / F_0(t)$, where $F_0(t)$ is the baseline fluorescence estimated as the 8% percentile value of the fluorescence distribution collected in a ±30 s window around each sample time point[44]. ROIs included in the analysis met the following criteria: the ROI size, defined by the number of pixels, was required to be between 40 and 150. The compactness of each ROI was quantified using the suite2p output "compact", which compares the ROI shape to that of a disk, leading to the exclusion of any ROI with a compactness value exceeding 1.1. In order to minimize contamination from neuropil signals, ROIs that exhibited a correlation coefficient greater than 0.8 with the neuropil fluorescence were also excluded. Furthermore, only those ROIs with a maximum ΔF/F value ranging from 1 to 10 and a minimum ΔF/F value above −1 were retained. Finally, to ensure adequate signal quality, an ROI was considered only if its signal-to-noise ratio (SNR) exceeded 0.3. To infer spiking activity using the deconvolution algorithm, ΔF/F traces were further refined by subtracting a baseline computed by applying a Gaussian filter with a width of 10 s, followed by minimum filtering and maximum filtering using a window size of 30 s. The baseline-subtracted ΔF/F traces were deconvolved using the OASIS AR1 model (minimum spike threshold = 0.3).

Functional network analysis

To assess the functional network, we computed pairwise partial correlation coefficients using deconvolved traces (smoothed with a Gaussian filter, σ = 0.26 s and z-scored) acquired over a 600 s recording period. In this analysis, we aimed to remove the influence of cortical-wide co-fluctuations by conditioning on the mean activity of all neurons. Denoting $x_i(t)$ and $x_j(t)$ as the smoothed deconvolved traces for neurons i and j, and letting $z(t)$ represent the mean activity of all neurons, the partial correlation between neurons i and j is given by

$$r_{ij,\,z} = \frac{r_{ij} - r_{iz} r_{jz}}{\sqrt{(1 - r_{iz}^2)(1 - r_{jz}^2)}}$$

where r_{ij} is the Pearson correlation coefficient between $x_i(t)$ and $x_j(t)$, r_{iz} is the Pearson correlation coefficient between $x_i(t)$ and $z(t)$, and r_{jz} is the Pearson correlation coefficient between $x_j(t)$ and $z(t)$. To compare inter-regional relationships across mice, we computed the mean partial correlation coefficient for each region in each mouse, then calculated the cosine similarity of these mean partial correlation vectors across mice. Spatial distributions of neuron-neuron links and degree distributions were analyzed by thresholding the partial correlation matrix at the 99th percentile to create a binary adjacency matrix.

Immunohistochemistry

Mice at postnatal 4 weeks were fixed by transcardial perfusion with 4% paraformaldehyde/0.1 M phosphate buffer. Fixed brains were sectioned at 50 μm with a vibratome (VT1200S, Leica). Coronal slices were successively subjected to 10% normal goat serum for 30 min, anti-GFAP rabbit antibody (RRID: AB_2571707, Nittobo Medical) overnight, and Alexa Fluor Plus 555-conjugated goat anti-rabbit secondary antibody (A32732, Thermo Fisher) for 2 h. Phosphate buffer saline with 0.1% Triton X-100 (PBST) was used for dilution and washing buffer. Images (1.27 × 1.27 mm) were taken with a confocal microscope (FV3000, Olympus) equipped with a 10x dry objective (UPLXAPO10X; numerical aperture = 0.4, working distance = 3.1 mm, Olympus) via a pinhole size of 1 airy unit and lateral resolution of 0.311 μm/pixel.

Quantification

Images were processed and analyzed with the ImageJ software (NIH). For a line scan analysis at single dendritic spines (Fig. 2c–e), the fluorescent intensity was measured using the plot profile function along a line of interest (3–4 μm in length) across the same dendritic spine in no treatment, SeeThrough, and open-skull windows with or without durotomy. A peak intensity and full width at half maximum (FWHM) were calculated from each dendritic spine using MATLAB software (MathWorks). The FWHM measures the width of a signal at half of its maximum amplitude. A narrower FWHM indicates a more concentrated signal, making it easier to distinguish from background noise. The signal-to-noise ratio is typically defined as the ratio of signal amplitude to the standard deviation of the noise. Thus, in optical imaging, where noise can appear as background fluorescence, a narrower FWHM suggests the signal peak is more distinct from the noise floor. In this study, we measured the FWHM of the same structure in SeeThrough and open-skull imaging experiments, comparing each value to assess the difference in the signal-to-noise ratio. To measure Iba1-tdTomato-labeled areas, the same imaging area (300 × 200 pixels) was selected between the SeeThrough and open-skull windows. Because the dura mater contains Iba1-labeled meningeal macrophages, preparations in which the dura remained intact (SeeThrough treatment and open-skull surgery without durotomy) exhibited higher basal Iba1-tdTomato fluorescence than open-skull surgery with durotomy. To measure GFAP-labeled areas, imaging areas (1610 × 805 pixels) were selected within 300 μm of the brain surface beneath the SeeThrough or open-skull window. Selected images were binarized with the same threshold to register regions of interest (ROIs) for Iba1-tdTomato- or GFAP-labeled areas. The total area of ROIs in individual images was measured. Four to twelve imaging areas for each experimental condition were obtained from two or three mice.

Statistical analysis

Blinding was not applied in this study. Data from all animals used in the experiments were included in the statistical analysis and data plots. Sample sizes were not predetermined with statistical methods. Quantitative data were presented as mean ± SD or mean ± SEM, as described in the figure legends. The details of sample number (n), including exact values, are indicated in the main text and/or figure legends. To compare two or more independent samples, the two-tailed Wilcoxon test or one-way ANOVA with the Tukey's multiple comparison test, Kruskal–Wallis test, Games–Howell test, Steel test, Mann–Whitney U-test, Fisher's exact test or Friedman test was used. To compare two or more paired samples, the two-tailed Wilcoxon test or one-way ANOVA with the Friedman test was used. To compare Kaplan–Meier survival curves, the log-rank test was used. A linear mixed-effects model was used to evaluate the effect of group and time on body weight, including their interaction (group × time) as a fixed effect and individual variability as a random effect. Statistical analyses were conducted using Prism 10 software (GraphPad Software). Differences between data sets were judged to be significant at $P < 0.05$.

Reporting summary. Further information on research design is available in the Nature Portfolio Reporting Summary linked to this article.

Data availability

Microscopic images presented or analyzed in this paper are publicly available at figshare (https://doi.org/10.6084/m9.figshare.26135071). The data sources are listed in Supplementary Data 5. All LC-MS raw and processed data in this paper are publicly available at figshare (https://doi.org/10.6084/m9.figshare.29589266). Any additional information required to reanalyze the data, such as experimental conditions and imaging parameters beyond those described in this manuscript, is available from the corresponding author. No custom code was generated in this study.

References

1. Wilt, B. A. et al. Advances in light microscopy for neuroscience. *Annu. Rev. Neurosci.* **32**, 435–506 (2009).
2. Svoboda, K. & Yasuda, R. Principles of two-photon excitation microscopy and its applications to neuroscience. *Neuron* **50**, 823–839 (2006).
3. Holtmaat, A. et al. Long-term, high-resolution imaging in the mouse neocortex through a chronic cranial window. *Nat. Protoc.* **4**, 1128–1144 (2009).
4. Xu, H. T., Pan, F., Yang, G. & Gan, W. B. Choice of cranial window type for in vivo imaging affects dendritic spine turnover in the cortex. *Nat. Neurosci.* **10**, 549–551 (2007).
5. Grutzendler, J., Kasthuri, N. & Gan, W. B. Long-term dendritic spine stability in the adult cortex. *Nature* **420**, 812–816 (2002).
6. Zhao, Y. J. et al. Skull optical clearing window for in vivo imaging of the mouse cortex at synaptic resolution. *Light Sci. Appl.* **7**, 17153 (2018).
7. Zhang, C. et al. A large, switchable optical clearing skull window for cerebrovascular imaging. *Theranostics* **8**, 2696–2708 (2018).
8. Li, D. et al. A Through-Intact-Skull (TIS) chronic window technique for cortical structure and function observation in mice. *eLight* **2**, 15 (2022).
9. Ascenzi, A. & Fabry, C. Technique for dissection and measurement of refractive index of osteones. *J. Biophys. Biochem. Cytol.* **6**, 139–142 (1959).
10. Berke, I. M., Miola, J. P., David, M. A., Smith, M. K. & Price, C. Seeing through musculoskeletal tissues: improving in situ imaging of bone and the lacunar canalicular system through optical clearing. *PloS ONE* **11**, e0150268 (2016).
11. Pan, C. et al. Shrinkage-mediated imaging of entire organs and organisms using uDISCO. *Nat. Methods* **13**, 859–867 (2016).
12. Tainaka, K. et al. Chemical landscape for tissue clearing based on hydrophilic reagents. *Cell Rep.* **24**, 2196–2210.e2199 (2018).
13. Ke, M. T. et al. Super-resolution mapping of neuronal circuitry with an index-optimized clearing agent. *Cell Rep.* **14**, 2718–2732 (2016).
14. Hansen, C. M. *Hansen Solubility Parameters: A User's Handbook* 2nd edn (CRC Press, 2007).
15. Murakami, T. C. et al. A three-dimensional single-cell-resolution whole-brain atlas using CUBIC-X expansion microscopy and tissue clearing. *Nat. Neurosci.* **21**, 625–637 (2018).
16. Zhang, Y. et al. Fast and sensitive GCaMP calcium indicators for imaging neural populations. *Nature* **615**, 884–891 (2023).
17. Mikuni, T., Nishiyama, J., Sun, Y., Kamasawa, N. & Yasuda, R. High-throughput, high-resolution mapping of protein localization in mammalian brain by in vivo genome editing. *Cell* **165**, 1803–1817 (2016).
18. Nishiyama, J., Mikuni, T. & Yasuda, R. Virus-mediated genome editing via homology-directed repair in mitotic and postmitotic cells in mammalian brain. *Neuron* **96**, 755–768.e755 (2017).
19. Chandrasekharan, N. V. et al. COX-3, a cyclooxygenase-1 variant inhibited by acetaminophen and other analgesic/antipyretic drugs: cloning, structure, and expression. *Proc. Natl Acad. Sci. USA* **99**, 13926–13931 (2002).
20. Nakayama, H. et al. Microglia permit climbing fiber elimination by promoting GABAergic inhibition in the developing cerebellum. *Nat. Commun.* **9**, 2830 (2018).
21. Sofroniew, M. V. & Vinters, H. V. Astrocytes: biology and pathology. *Acta Neuropathol.* **119**, 7–35 (2010).
22. Dorand, R. D., Barkauskas, D. S., Evans, T. A., Petrosiute, A. & Huang, A. Y. Comparison of intravital thinned skull and cranial window approaches to study CNS immunobiology in the mouse cortex. *Intravital* **3**, e29728 (2014).
23. Kierdorf, K., Masuda, T., Jordão, M. J. C. & Prinz, M. Macrophages at CNS interfaces: ontogeny and function in health and disease. *Nat. Rev. Neurosci.* **20**, 547–562 (2019).
24. Jessen, N. A., Munk, A. S., Lundgaard, I. & Nedergaard, M. The glymphatic system: a beginner's guide. *Neurochem. Res.* **40**, 2583–2599 (2015).
25. Rustenhoven, J. & Kipnis, J. Brain borders at the central stage of neuroimmunology. *Nature* **612**, 417–429 (2022).
26. Nedergaard, M. & Goldman, S. A. Glymphatic failure as a final common pathway to dementia. *Science* **370**, 50–56 (2020).
27. Feng, G. et al. Imaging neuronal subsets in transgenic mice expressing multiple spectral variants of GFP. *Neuron* **28**, 41–51 (2000).
28. Hattori, R. & Komiyama, T. Longitudinal two-photon calcium imaging with ultra-large cranial window for head-fixed mice. *STAR Protoc.* **3**, 101343 (2022).
29. Kim, T. H. et al. Long-term optical access to an estimated one million neurons in the live mouse cortex. *Cell Rep.* **17**, 3385–3394 (2016).
30. Kyweriga, M., Sun, J., Wang, S., Kline, R. & Mohajerani, M. H. A large lateral craniotomy procedure for mesoscale wide-field optical imaging of brain activity. *J. Vis. Exp.* 52642 (2017).
31. Oomoto, I. et al. Protocol for cortical-wide field-of-view two-photon imaging with quick neonatal adeno-associated virus injection. *STAR Protoc.* **2**, 101007 (2021).
32. Ota, K. et al. Fast, cell-resolution, contiguous-wide two-photon imaging to reveal functional network architectures across multi-modal cortical areas. *Neuron* **109**, 1810–1824.e1819 (2021).
33. Shiba, Y. et al. Allogeneic transplantation of iPS cell-derived cardiomyocytes regenerates primate hearts. *Nature* **538**, 388–391 (2016).

34. Yatsenko, D. et al. Improved estimation and interpretation of correlations in neural circuits. *PLoS Comput. Biol.* **11**, e1004083 (2015).
35. Perin, R., Berger, T. K. & Markram, H. A synaptic organizing principle for cortical neuronal groups. *Proc. Natl Acad. Sci. USA* **108**, 5419–5424 (2011).
36. Ueda, H. R. et al. Tissue clearing and its applications in neuroscience. *Nat. Rev. Neurosci.* **21**, 61–79 (2020).
37. Weller, R. O., Sharp, M. M., Christodoulides, M., Carare, R. O. & Møllgård, K. The meninges as barriers and facilitators for the movement of fluid, cells and pathogens related to the rodent and human CNS. *Acta Neuropathol.* **135**, 363–385 (2018).
38. Plog, B. A. et al. When the air hits your brain: decreased arterial pulsatility after craniectomy leading to impaired glymphatic flow. *J. Neurosurg.* **133**, 210–223 (2020).
39. Qin, Z. et al. Deep tissue multi-photon imaging using adaptive optics with direct focus sensing and shaping. *Nat. Biotechnol.* **40**, 1663–1671 (2022).
40. Wang, T. et al. Three-photon imaging of mouse brain structure and function through the intact skull. *Nat. Methods* **15**, 789–792 (2018).
41. Tervo, D. G. et al. A designer AAV variant permits efficient retrograde access to projection neurons. *Neuron* **92**, 372–382 (2016).
42. Kobayashi, K. et al. Survival of corticostriatal neurons by Rho/Rho-kinase signaling pathway. *Neurosci. Lett.* **630**, 45–52 (2016).
43. Pachitariu, M. et al. Suite2p: beyond 10,000 neurons with standard two-photon microscopy. Preprint at *bioRxiv* https://doi.org/10.1101/061507 (2017).
44. Dombeck, D. A., Khabbaz, A. N., Collman, F., Adelman, T. L. & Tank, D. W. Imaging large-scale neural activity with cellular resolution in awake, mobile mice. *Neuron* **56**, 43–57 (2007).

Acknowledgements

The authors thank L. Colgan for critical reading of the manuscript; the K.T. and T.M. lab members and H. Ueda for discussion; and N. Saito, Y. Sakaki, A. Sakaki, Y. Nakagami, and M. Isogai for technical assistance. This work was supported by Grants-in-Aid for Scientific Research (JP20H05914, JP20H05918, JP23K18160, and JP24K02130 to M.U.; JP24H02313 and JP20H05775 to M.M.; JP22H02937 and JP22K19105 to K.T.; and JP22K21353, JP23H04672, JP23H02574, JP23K27265, JP24H01229, JP24K22000, and JP25H02490 to T.M.), Japan Agency for Medical Research and Development (AMED) (JP15dm0207001 and JP23wm0625001 to M.M.; JP21wm0425001, JP21zf0127004 and JP24wm0625117 to K.T.; and JP19dm0207080, JP21wm0525014 and JP24wm0625117 to T.M.), Japan Science and Technology Agency (JST) (JPMJFR231M to M.U.), Human Frontier Science Program (CDA00043/2019-C to T.M.), Kowa Life Science Foundation (M.U.), Narishige Neuroscience Research Foundation (M.U.), Uehara Memorial Foundation (T.M.), TORAY Science Foundation (M.M. and T.M.), Takeda Science Foundation (T.M.), RIKEN Incentive Research Projects (M.M.), and Brain Science Foundation (T.M.).

Author contributions

Conceptualization: K.T. and T.M.; Methodology: K.T. and T.M.; Investigation: X.L., M.U., I.O., Y.Saito, H.U., S.O., K.M., D.S., Y.Shimizu, and M.M.; Formal analysis: X.L., M.U., I.O., Y.Saito, H.U., S.O., K.M., Y.Shimizu, M.M., K.T., and T.M.; Visualization: X.L., M.U., I.O., Y.Saito, M.M., K.T., and T.M.; Resources: M.A. and K.S.; Funding acquisition: M.U., M.M., K.T., and T.M.; Project administration: K.T. and T.M.; Supervision: K.T. and T.M.; Writing—original draft: M.U., I.O., Y.Saito, M.M., K.T., and T.M.; and Writing—review & editing: T.M. All authors contributed to the discussion to finalize the manuscript.

Competing interests

X.L., M.U., K.T., and T.M. are inventors on a patent application that covers the methodological development of the SeeThrough technique. The applicant is Niigata University, and the application number is PCT/JP2025/012465. The application is currently pending. The authors declare no other competing interests.

Additional information

Supplementary information The online version contains supplementary material available at https://doi.org/10.1038/s41467-025-62836-1.

Correspondence and requests for materials should be addressed to Masanori Murayama, Kazuki Tainaka or Takayasu Mikuni.

Peer review information *Nature Communications* thanks the anonymous reviewer(s) for their contribution to the peer review of this work. A peer review file is available.